Retrofit Control of Wind-Integrated Power Systems

Tomonori Sadamoto[1], *Member, IEEE,* Aranya Chakrabortty[2], *Senior Member, IEEE,* Takayuki Ishizaki[1], *Member, IEEE,* and Jun-ichi Imura[1] *Member, IEEE,*

Abstract—In this paper we address several growing concerns of wind power integration from the perspective of power system dynamics and stability. We propose a new control design technique called retrofit control by which one can control the rotor voltages of doubly-fed induction generators to suppress the oscillations in the tie-line power flows caused by a disturbance inside the wind farm. The controller can be designed in a modular way, and also implemented in a completely decentralized fashion using only local feedback from the wind generator states and the voltage at the point of common coupling without depending on the states of any of the synchronous machines in the rest of the system. We show the effectiveness of the design using simulations of the IEEE 68- bus, 16-machine power system model with two wind farms.

Index Terms—Wind integration, small-signal stability, decentralized control, damping, DFIG, retrofit control

NOMENCLATURE

The variables below are in per unit unless otherwise stated. Wherever necessary, we will use the subscript k for these symbols to denote that they belong to the k-th bus.

Power Network:

$\bar{\omega}$	Base frequency, which is 120π (rad/sec)
$\mathbb{N}$	index set of all buses
$\mathbb{N}_G, \mathbb{N}_L, \mathbb{N}_W$	index set of generator bus, load bus, and wind farm bus
V, θ	voltage magnitude and angle of a bus
P, Q	active and reactive power flowing to a bus
$\bar{P}, \bar{Q}$	constant active and reactive power consumed by load
$\mathbf{Y}$	admittance matrix

Synchronous Generators:

δ	rotor angle (rad)
ω	rotor frequency
E	internal voltage of rotor
V_{fd}	voltage of the excitation winding
P_{m}	mechanical power input
V_{pss}	output voltage of Power System Stabilizer (PSS)
M, d	inertia (sec) and damping coefficient of rotor
τ_{o}	open-circuit time constant (sec)
$\tau_{\mathrm{a}}, K_{\mathrm{a}}$	regulator time constant (sec) and gain
x_{d}	d-axis synchronous reactance
x_{d}'	d-axis transient reactance
ζ_{pss}	PSS state vector

Wind Farm:

$\omega_{\mathrm{r}}, \omega_{\mathrm{g}}$	turbine and generator frequency
θ_{T}	generator torsion angle (rad)
T	torque used by DFIG
P_{a}	aerodynamic power input
$J_{\mathrm{r}}, J_{\mathrm{g}}$	inertia of turbine and generator (sec)
$B_{\mathrm{r}}, B_{\mathrm{g}}$	friction coefficients of turbine and generator
K_{c}	torsional stiffness (1/rad)
d_{c}	torsion damping
N_{g}	gear ratio
$i_{\mathrm{dr}}, i_{\mathrm{qr}}$	d- and q-axis rotor currents
$i_{\mathrm{ds}}, i_{\mathrm{qs}}$	d- and q-axis stator currents
$v \in \mathbb{R}^2$	d- and q-axis rotor voltage
$x_{\mathrm{s}}, x_{\mathrm{r}}$	stator, rotor reactance
x_{m}	magnetizing reactance
$r_{\mathrm{s}}, r_{\mathrm{r}}$	stator, rotor resistances
γ	number of wind generators
$\zeta_{\mathrm{dI}}, \zeta_{\mathrm{qI}}$	state of d- and q-axis internal controller
$v_{\mathrm{d}}, v_{\mathrm{q}}$	d- and q-axis output voltage of internal controller
$K_{\mathrm{dP}}, K_{\mathrm{dI}}$	PI gains of d-axis internal controller
$K_{\mathrm{qP}}, K_{\mathrm{qI}}$	PI gains of q-axis internal controller
z	state vector of wind farm

Retrofit Controller:

ξ	state of retrofit controller
u	input generated by retrofit controller
$\hat{n}$	dimension of retrofit controller

All variables with superscript $\star$ denote setpoints (e.g., $i_{\mathrm{dr}}^\star$ is the setpoint reference for i_{dr}).

Mathematical Notation: We denote the imaginary unit by $j := \sqrt{-1}$, the set of real numbers by $\mathbb{R}$, the set of complex numbers by $\mathbb{C}$, the cardinality of a set $\mathcal{I}$ by $|\mathcal{I}|$, the pseudoinverse of a full-column rank matrix W by $W^\dagger$, and the n-dimensional identity matrix by I_n. The system $\dot{x} = f(x, u)$, where u is input, is said to be stable if the autonomous system under $u = 0$ is exponentially stable. We denote the $\mathcal{L}_2$-norm of a square-integrable function $f(\cdot)$ by $\|f(t)\|_{\mathcal{L}_2} := \sqrt{\int_0^\infty \|f(t)\|^2 dt}$.

I. INTRODUCTION

Recent papers such as [1], [2], [3], [4] have shown how large-scale wind penetration can have concerning impacts on the transient stability and small-signal stability of large power system networks. Although the asynchronous active power flows resulting from wind generation can help in maintaining rotor-angle stability, the corresponding reactive

[1]Department of Systems and Control Engineering, Graduate School of Engineering, Tokyo Institute of Technology; 2-12-1, Meguro, Tokyo, Japan;
[2]Electrical & Computer Engineering, North Carolina State University; Raleigh, NC 27695
{sadamoto, ishizaki, imura}@sc.e.titech.ac.jp
achakra2@ncsu.edu

power injections can overburden the synchronous generators, resulting in undesired angular separations between their phase angles. Such separations happen not only in steady state, but also during transient behavior [5], [6], owing largely to the heterogeneous dynamic models of doubly-fed induction generators (DFIG) placed in between the homogeneous swing dynamics of synchronous machines. Currently, wind power system operators tend to mitigate these types of stability threats by simply tuning PID controllers that are used for setpoint regulation of active and reactive power outputs of DFIGs [7], [8]. However, when the wind penetration level is high, such ad-hoc tuning itself may end up destabilizing the overall power system as shown in [9]. An alternative option would be to design a system-wide damping controller using power system stabilizers (PSSs), but such a design can easily become intractable due to increasing transmission expansion. What operators really need is a systematic control mechanism on the wind side by which they can regulate wind farms at high wind penetration levels without destabilizing the overall power system. This controller should preferably be *modular*, meaning that it should be driven by local output feedback from the wind farm only, and neither its design nor its actuation should depend on any information from the rest of the system.

These design preferences perfectly fit the concept of *retrofit* control, which was recently introduced in [10], [11]. The idea behind retrofit control is as follows. Imagine a pre-existing network of dynamic agents operating with internal stabilizing controllers. Say, a new agent, with potentially heterogeneous dynamics, is added to this network in a way that it destabilizes the network model. One option to mitigate this would be to redesign every single controller of the pre-existing network from scratch so that they can safely accommodate the new node. However, such redesigns can be extremely tedious and computationally expensive when the pre-existing network has tens of hundreds of nodes just like in a power system. In contrast, the retrofitting approach needs information about the model of the new agent only, and designs a controller using local feedback from only its internal states and the output that couples its dynamics with that of the pre-existing network. The design in [10], [11] showed that such a local controller can not only guarantee stability, but can also improve dynamic performance of the closed-loop system with the new agent accommodated.

In this paper we show how the idea of retrofit control can be used for ensuring small-signal stability as well as enhancing damping of the electro-mechanical states in a wind-integrated power system. The pre-existing network here comprises of multiple synchronous generators and constant power loads while the newly added components are multiple wind farms, each containing multiple wind turbines, converters, and DFIGs. The design process can be summarized as follows. First, we consider the wind-integrated system without any retrofit controller, and ensure that the PSS gains of the synchronous generators are robust enough to stabilize the entire power system model for a given penetration level of wind power. Note that the objective of this step is only to come up with a set of PSS gains that guarantee the stability of the entire power system; we do not require any PSS tuning here

to optimize the dynamic performance of the system. Second, we consider each wind farm to be isolated from the rest of the system, and hypothetically connected to an infinite bus, and design a retrofit controller for that farm using a linear quadratic regulator (LQR) that depends on partial feedback of the wind farm state only. The controller is actuated through the current control loop of the DFIG in parallel to pre-existing PI controllers that are used for setpoint regulation of these currents. Finally, the synchronous generators with the chosen PSS gains are integrated with the wind farms and the chosen LQR-based retrofit controllers, and the transient response of the frequency and power flow oscillations of the integrated system are shown to improve significantly. The results are validated by simulations of the designed controller on the 68-bus IEEE test system model [12] with two wind farms.

Some preliminary results on this topic have been recently presented in our conference paper [9]. The design in this paper, however, is far more advanced in comparison as it accommodates specific frequencies at which the DFIG is shown to cause resonance, a very important design aspect that was not captured in [9]. The simulations and the resulting insights in [9] were limited to only a simple 9-bus Kundur model with a single wind farm, whereas here they are presented for a significantly larger 68-bus system with multiple wind farms that sheds more light on the structural requirements of the retrofit controller. We also show how the controller can be made lower-dimensional without serious loss of performance, which was not considered in [9].

The rest of the paper is organized as follows. In Section II, we recall the dynamic model of a power system with synchronous generators, loads, and wind farms. In Section III, we show an example that illustrates how wind penetration can induce oscillatory behavior in the line flows after a certain limit. In order to enhance the damping performance, Section IV proposes, based on [10], [11], a retrofit controller for each wind farm. In Section V, we demonstrate the efficiency of the controllers on a 68-bus power system model. Finally, concluding remarks are provided in Section VI.

II. SIGNAL-FLOW DIAGRAMS OF WIND-INTEGRATED POWER SYSTEMS

We recall the dynamic model of a power system network, consisting of synchronous generators, loads, and wind farms. The bus index sets of these three components are denoted as $\mathbb{N}_G$, $\mathbb{N}_L$, and $\mathbb{N}_W$. While these models are standard in literature [7], [13], restating them at the outset of this paper is very important for the purpose of creating their *signal-flow* diagrams, all of which will be critical for deriving the structural properties of retrofit control. For simplicity, we consider the loads to be constant power loads, and each wind farm to be modeled by the combination of a single aggregate turbine, an aggregate DFIG, and an internal controller. Neither of these assumptions, however, are necessary for our design.

A. Synchronous Generators and Loads

For $k \in \mathbb{N}_G$, the dynamics of the synchronous generator connecting to the k-th bus can be written as a combination of
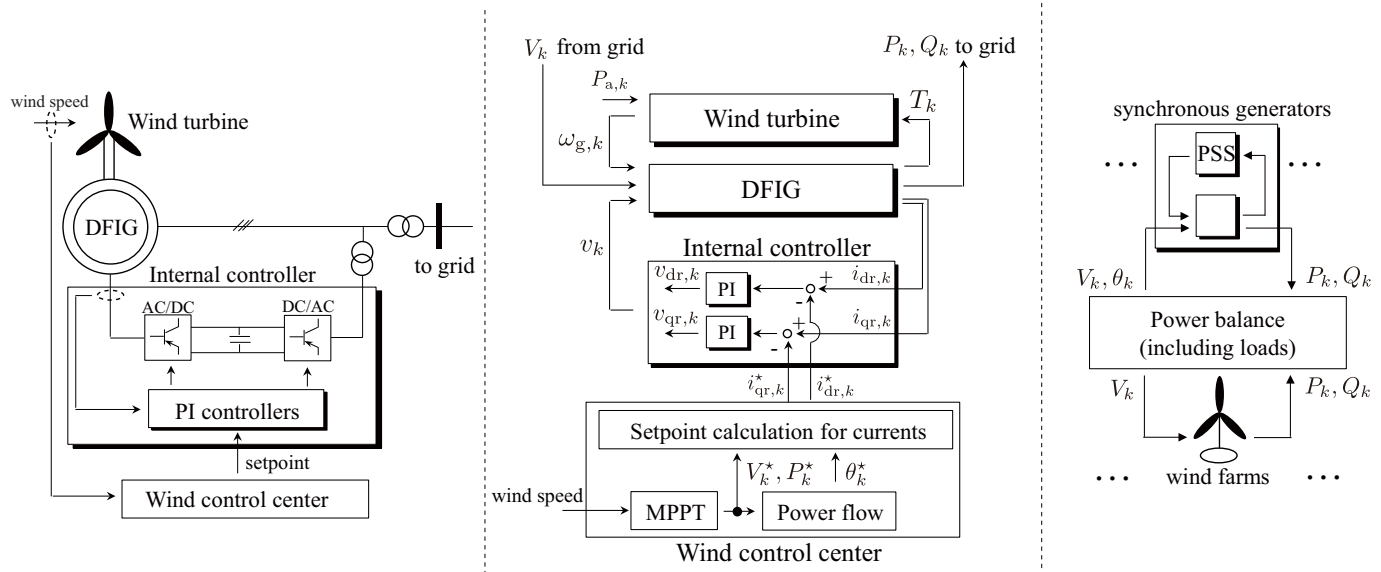
Fig. 1. (Left) Physical components of the wind power plant. (Middle) Signal-flow diagram of the wind farm model. (Right) Signal-flow diagram of the wind-integrated power system whose mathematical model is defined by (1)-(10).

the electro-mechanical swing dynamics [6]

$$\begin{cases} \dot{\delta}_k = \bar{\omega}\omega_k \\ M_k\dot{\omega}_k = P_{m,k} - d_k\omega_k - \frac{V_kE_k}{x'_{d,k}}\sin(\delta_k - \theta_k) \end{cases} \quad (1)$$

and the electro-magnetic excitation dynamics

$$\begin{cases} \tau_{o,k}\dot{E}_k = -\frac{x_{d,k}}{x'_{d,k}}E_k + (\frac{x_{d,k}}{x'_{d,k}} - 1)V_k\cos(\delta_k - \theta_k) + V_{fd,k} \\ \tau_{a,k}\dot{V}_{fd,k} = -V_{fd,k} - K_{a,k}(V_k - V_k^\star - V_{pss,k}). \end{cases} \quad (2)$$

We assume the mechanical power input $P_{m,k}$ to be constant. The active and reactive power outputs can be written as

$$\begin{cases} P_k = \frac{E_kV_k}{x'_{d,k}}\sin(\delta_k - \theta_k) \\ Q_k = \frac{1}{x'_{d,k}}\left(E_kV_k\cos(\delta_k - \theta_k) - V_k^2\right). \end{cases} \quad (3)$$

Typically, generators are equipped with Automatic Voltage Regulators (AVRs) and PSSs to ensure small-signal stability. We model a PSS as a typical speed-feedback controller [12]

$$\begin{cases} \dot{\zeta}_{pss,k} = A_{pss,k}\zeta_{pss,k} + B_{pss,k}\omega_k \\ V_{pss,k} = C_{pss,k}\zeta_{pss,k} + D_{pss,k}\omega_k \end{cases} \quad (4)$$

where the matrices in (4) are summarized in the appendix.

For $k \in \mathbb{N}_L$, the k-th load is supposed to consume constant power at any time, i.e.,

$$P_k(t) \equiv \bar{P}_k, \quad Q_k(t) \equiv \bar{Q}_k. \quad (5)$$

B. Wind Farms

For $k \in \mathbb{N}_W$, the wind farm connected to the k-th bus is considered to be an aggregation of multiple wind generators inside the wind farm. Following standard literature such as [14], the model of all the generators and turbines are assumed to be identical. Under this assumption, the wind farm can be modeled as a single wind generator whose dynamics are identical to that of each generator, and the total power injected

into the grid is the sum of the power output of each individual generator. The aggregate model has a wind turbine, a DFIG, and an internal current controller, whose physical structure is shown in the leftmost subfigure of Fig. 1. The internal controller consists of a PI-regulator, cascaded with an actuator in the form of a back-to-back (B2B) converter. The state-space model of a B2B converter typically consists of three source-side currents, three load-side currents, and one DC link capacitor voltage. Details of this model can be found in [15]. For simplicity, we skip rewriting that model since its time-constant is much faster than that of the electro-mechanical dynamics (1), as a result of which we will ignore the converter dynamics in our proposed control design.

Following [16], the wind turbine model can be written as

$$\begin{cases} J_{r,k}\dot{\omega}_{r,k} = -(d_{c,k} + B_{r,k})\omega_{r,k} + \frac{d_{c,k}}{N_{g,k}}\omega_{g,k} - K_{c,k}\theta_{T,k} + \frac{P_{a,k}}{\omega_{r,k}} \\ J_{g,k}\dot{\omega}_{g,k} = \frac{d_{c,k}}{N_{g,k}}\omega_{r,k} - \left(\frac{d_{c,k}}{N_{g,k}^2} + B_{g,k}\right)\omega_{g,k} + \frac{K_{c,k}}{N_{g,k}}\theta_{T,k} - T_k \\ \dot{\theta}_{T,k} = \bar{\omega}\left(\omega_{r,k} - \frac{1}{N_{g,k}}\omega_{g,k}\right). \end{cases} \quad (6)$$

Representative values of the model parameters are provided in the appendix. The aerodynamic power input $P_{a,k}$ is assumed to be constant owing to its slow temporal variation.

The DFIG in the middle subfigure of Fig. 1 is modeled through the dynamics of its stator and rotor currents, in a similar way as in [17], expressed in a rotating d-q reference frame as

$$\begin{cases} \dot{i}_k = A_{i,k}(\omega_{g,k})i_k + R_{i,k}V_k + B_{i,k}v_k \\ T_k = x_{m,k}(i_{ds,k}i_{qr,k} - i_{qs,k}i_{dr,k}) \\ P_k = \gamma_k V_k i_{qs,k} \\ Q_k = \gamma_k V_k i_{ds,k} \end{cases}, \quad i_k := \begin{bmatrix} i_{dr,k} \\ i_{qr,k} \\ i_{ds,k} \\ i_{qs,k} \end{bmatrix}. \quad (7)$$

The exact expressions of the matrices in (7) and the values of the model parameters are provided in the appendix. In (7), γ_k denotes the number of wind generators inside the wind
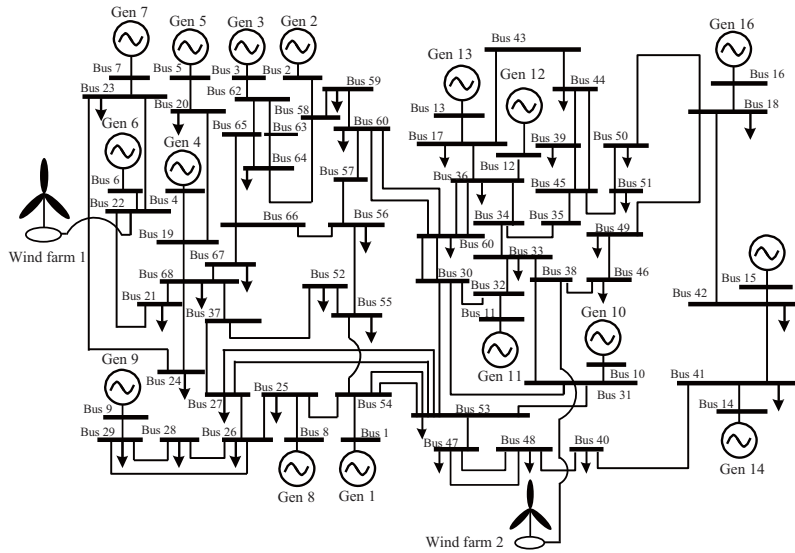
Fig. 2. IEEE 68-bus, 16-machine power system model with two wind farms at Bus 22 and 38.
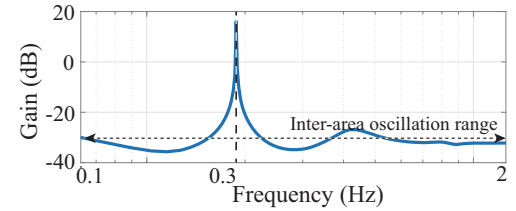

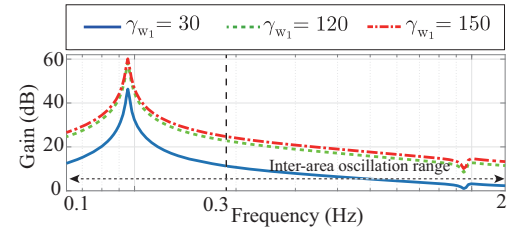Fig. 3. Bode gain diagram of the transfer function from the power output of the first wind farm to its bus voltage

Fig. 4. Bode gain diagram of the transfer function from the bus voltage of the first wind farm to its generated power

farm connecting to the k-th bus. Hence, a larger value of γ_k indicates that a larger amount of wind power is injected to the grid. Later in our simulations we will numerically inspect the influence of this penetration level on the transient stability and dynamic performance of the IEEE 68-bus test system.

Typically, the d- and q-axis rotor voltage $v_k = [v_{\mathrm{d},k} v_{\mathrm{q},k}]^\mathsf{T}$ is controlled by regulating the d- and q-axis rotor currents to pre-computed setpoints $i^\star_{\mathrm{dr},k}$, $i^\star_{\mathrm{qr},k}$. Those setpoints are calculated based on three quantities - namely, the steady-state voltage magnitude of the wind bus (PV bus), the steady-state voltage angle of the wind bus that is computed from power flow, and the steady-state active power of the wind bus, which is computed from a maximum power-point tracking (MPPT) algorithm based on wind speed. The regulation of the rotor currents to their setpoints is achieved by PI control as

$$\begin{cases} \dot{\zeta}_{\mathrm{dI},k} = K_{\mathrm{dI},k}(i_{\mathrm{dr},k} - i^\star_{\mathrm{dr},k}) \\ v_{\mathrm{d},k} = K_{\mathrm{dP},k}(i_{\mathrm{dr},k} - i^\star_{\mathrm{dr},k}) + \zeta_{\mathrm{dI},k} \end{cases}$$
$$\begin{cases} \dot{\zeta}_{\mathrm{qI},k} = K_{\mathrm{qI},k}(i_{\mathrm{qr},k} - i^\star_{\mathrm{qr},k}) \\ v_{\mathrm{q},k} = K_{\mathrm{qP},k}(i_{\mathrm{qr},k} - i^\star_{\mathrm{qr},k}) + \zeta_{\mathrm{qI},k}. \end{cases} \tag{8}$$

We limit the control loop for our wind farm model to (8) only. Other control loops such as converter controls and reactive power control are ignored for the sake of reducing unnecessary complexity as those control loops have very little sensitivity towards damping of electro-mechanical oscillations [8].

C. Interconnection of Buses

The dynamics of the wind farms, synchronous generators, and loads are interconnected through power flow balance

$$\mathbf{P} + j\mathbf{Q} = (\mathbf{Y}\mathbf{V})^* \times \mathbf{V} \tag{9}$$

where $\mathbf{P} \in \mathbb{R}^{|\mathbb{N}|}$, $\mathbf{Q} \in \mathbb{R}^{|\mathbb{N}|}$ and $\mathbf{V} \in \mathbb{C}^{|\mathbb{N}|}$ are the stacked representations of P_k, Q_k and $V_k(\cos\theta_k + j\sin\theta_k)$, and the symbol $\times$ denotes element-wise multiplication. Buses that do

not connect to any synchronous generators, loads, or wind farm, but only to other buses, must satisfy

$$P_k = 0, \quad Q_k = 0, \quad k \in \mathbb{N} \setminus (\mathbb{N}_\mathrm{G} \cup \mathbb{N}_\mathrm{L} \cup \mathbb{N}_\mathrm{W}). \tag{10}$$

Equations (1)-(10) represent the overall power system model of our interest. The signal-flow diagram of this is shown in the rightmost subfigure in Fig. 1. The part of this model without considering the wind farms is referred to as the *pre-existing grid* model. This nomenclature acknowledges that we treat the grid with conventional synchronous generation as a nominal system, and the wind farms as new components to be added to this nominal system.

III. MOTIVATING EXAMPLE

We next consider the IEEE 68-bus power system model with 16 synchronous generators [12] and two wind farms connected to Bus 22 and Bus 38, as shown in Fig. 2. Thus, $\mathbb{N}_\mathrm{W} = \{22, 38\}$. Assume the number of wind generators inside the two farms to be $\gamma_{\mathrm{w}_1} = 30$ and $\gamma_{\mathrm{w}_2} = 100$. We also suppose that the PI gains of the internal controller are $K_{\mathrm{dP},k} = K_{\mathrm{qP},k} = 10$ and $K_{\mathrm{dI},k} = K_{\mathrm{qI},k} = 1$ in (8) for $k \in \mathbb{N}_\mathrm{W}$. The PSSs in (4) are designed such that the entire power system model (1)-(10) is stable, where the values of PSS parameters are shown in the appendix. We linearize the first wind farm as well as the rest of the grid excluding this wind farm. We consider the 2×1 transfer matrix of the grid considering the input as the voltage magnitude of the wind bus 22, and the outputs as the active and reactive power flowing from this bus into the grid. Fig. 3 shows the maximum element-wise Bode gain of this transfer matrix. The figure shows a resonance peak at 0.3 (Hz). Fig. 4, on the other hand, shows the maximum Bode gain of the linearized model of the first wind farm where the input is the power injected by the grid, and the output is the wind bus voltage magnitude. This figure shows a resonance peak at around 0.16 (Hz) following from the typical values of the poles of the DFIG model in (7).
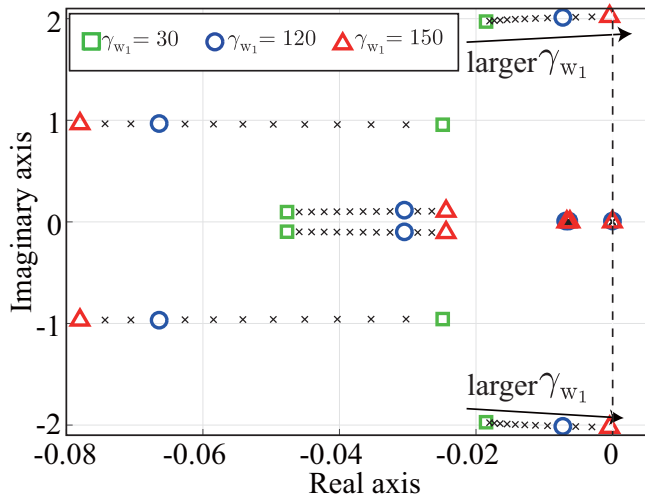
Fig. 5. Variation of the first nine dominant eigenvalues of the linearized wind-integrated system for different values of γ_{w_1}
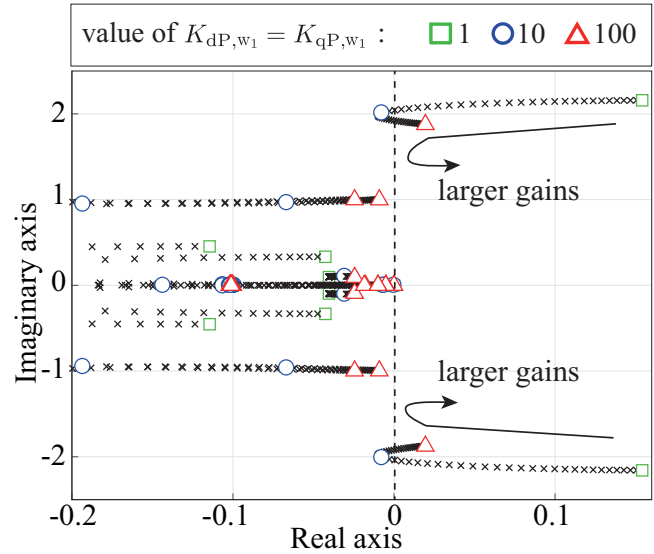

Fig. 6. Variation of the first thirteen dominant eigenvalues of the linearized wind-integrated power system for different values of the P gains of the internal controller for the first wind farm

The Bode gain at 0.3 (Hz) is around 16 (dB) when $\gamma_{w_1} = 30$. By increasing the value of γ_{w_1}, the gain at this frequency increases monotonically, as shown by the green broken and red dot-dashed lines in Fig. 4. These two figures indicate that the wind farm stimulates a strong resonance peak in the dynamics of the rest of the grid at around a frequency of 0.3 (Hz), which falls in the range of inter-area oscillations. With increasing values of γ_{w_1}, the entire power system becomes oscillatory with poor damping of the inter-area modes. This observation was also shown in a slightly different context in the recent paper [6]. Fig. 5 shows the first nine dominant eigenvalues of the linearized closed-loop model (1)-(10). The eigenvalues around $-0.019 \pm 1.97j$ for $\gamma_{w_1} = 30$ start moving to the right as the value of γ_{w_1} is increased, and finally cross the imaginary axis when $\gamma_{w_1} > 150$, resulting in a completely unstable system. In summary, this example shows that very high levels of wind penetration can induce transient oscillations in power flows, and may even result in small-signal instability of the entire power system after a certain limit. This phenomenon is independent of the number of wind farms, and is observed even when the second wind farm is not present.

One potential way to combat this oscillatory behavior would be to tune the PI gains of the DFIG current controller in (8). However, such tuning must be done extremely carefully with full knowledge of the entire closed-loop model (1)-(10), since both low and high values of these gains can jeopardize closed-loop stability. This is shown in Fig. 6, where the first thirteen dominant eigenvalues of the linearized closed-loop model for $\gamma_{w_1} = 120$ are shown. P gains that are less than 8 or more than 27 end up destabilizing the power system. This is because low-gain controllers cannot sufficiently mitigate the adverse impacts of the resonance peak observed in Fig. 4, while high-gain controllers stimulate the negative coupling effect coming from the pre-existing grid. Similar phenomenon can be observed by tuning the integral gains as well.

These observations motivate us for building a much more systematic mechanism by which the negative impacts of wind penetration on power system dynamics can be regulated in a desired way without posing any threats of instability. In the next section we propose such a mechanism using the idea of retrofit control.

IV. RETROFIT CONTROL

To combat the destabilizing effects of wind penetration shown in Fig. 5, we design a supplementary controller called *retrofit controller* on top of the PI-controller (8) for the DFIG. The rotor voltage in (7) is, therefore, expressed as

$$v_k = [v_{\mathrm{d},k}, v_{\mathrm{q},k}]^\mathsf{T} + u_k \tag{11}$$

where u_k is an additional control input, and $v_{\mathrm{d},k}$ and $v_{\mathrm{q},k}$ are the output of the internal controller (8). For the rest of this section, all the symbols having the subscript k are defined for $k \in \mathbb{N}_\mathrm{W}$. We write the wind farm model in (6), (7), (8) and (11) in a compact form as

$$\dot{z}_k = F_k(z_k; i_{\mathrm{r},k}^\star) + R_k V_k + B_k u_k \tag{12}$$

where $i_{\mathrm{r},k}^\star := [i_{\mathrm{dr},k}^\star, i_{\mathrm{qr},k}^\star]^\mathsf{T}$, and

$$z_k := \begin{bmatrix} \omega_{\mathrm{r},k} \\ \omega_{\mathrm{g},k} \\ \theta_{\mathrm{T},k} \\ i_k \\ \zeta_{\mathrm{dI},k} \\ \zeta_{\mathrm{qI},k} \end{bmatrix} \in \mathbb{R}^9, \ R_k := \begin{bmatrix} 0 \\ 0 \\ 0 \\ R_{\mathrm{i},k} \\ 0 \\ 0 \end{bmatrix}, \ B_k := \begin{bmatrix} 0 \\ 0 \\ 0 \\ B_{\mathrm{i},k} \\ 0 \\ 0 \end{bmatrix},$$

and $F_k(\cdot; \cdot)$ follows from (6), (7), (8) and (11).

Definition 1: We define $\mathcal{P}$ to be the combination of (1)-(5), (9), (10), (11), and (12), representing the wind-integrated power system with the additional control input u_k for all $k \in \mathbb{N}_\mathrm{W}$.

We impose the following assumptions on $\mathcal{P}$.

Assumption 1: The internal controllers in (8) and PSSs in (4) ensure the stability of $\mathcal{P}$ when $u_k = 0$ for every $k \in \mathbb{N}_W$.

As pointed out in the introduction, this assumption only requires stability of the (pre-existing grid + wind farms) model. No assumption is required for its dynamic performance.

Assumption 2: For every $k \in \mathbb{N}_W$, the wind state vector z_k and the wind bus voltage V_k are assumed to be measurable.

Both of these assumptions hold in common practice. Under these assumptions, we consider designing u_k in (12) using the concept of retrofit control [10], [11]. Before stating the actual design, we quickly list the two main requirements from the controllers:

i) The controllers should preserve closed-loop stability, and also improve the damping of the synchronous generator frequencies and line flows.

ii) Each of the controllers should depend only on local state feedback from the corresponding wind farm, and not on any states from the rest of the grid including other wind farms. Each of the controllers should also be designed independent of the model of the rest of the system.

Property (ii) is most important as otherwise one would have to know a very accurate model of the entire power system, which is often impractical owing to the sheer size and complexity of the network. Property (ii) implies that each controller should be modular by design, and decentralized by implementation. Following [10], [11], we consider the input u_k to be composed of two parts, namely

$$u_k = u_{1,k} + u_{2,k}. \tag{13}$$

The component $u_{1,k}$ is designed under two hypothetical and yet simplifying assumptions as follows:

a) the nonlinearity $F_k(z_k; \cdot)$ in (12) is approximated by using its first-order derivative defined as

$$A_k := \frac{\partial F_k}{\partial z_k}(z_k^\star; i_{r,k}^\star), \tag{14}$$

b) every wind farm is disconnected from the rest of the grid, which means that the coupling term $V_k = 0$ for all $k \in \mathbb{N}_W$.

Note that these two assumptions are only made to simplify the design of u_k. They do not influence the actual implementation of the control. Under these assumptions, $u_{1,k}$ in (13) can be simply designed as

$$u_{1,k} = K_k z_k \tag{15}$$

where K_k is designed so that $A_k + B_k K_k$ is Hurwitz. However, in reality neither of these assumptions will be true. Thus, if we only implement $u_k = u_{1,k}$, then this control will pose serious threat to stability for neglecting the dynamics following from the nonlinearity $F_k(z_k; i_{r,k}^\star) - A_k z_k$, and for neglecting the dynamics of the rest of the grid excluding the wind farm via V_k, both of which will be stimulated by the control. In order to prevent this stimulation, we create the compensation signal $u_{2,k}$ in (13) by a dynamical compensator

$$\Sigma_k : \begin{cases} \dot{\xi}_k = A_k \xi_k + f_k(z_k; i_{r,k}^\star) + R_k V_k \\ u_{2,k} = -K_k \xi_k \end{cases} \tag{16}$$
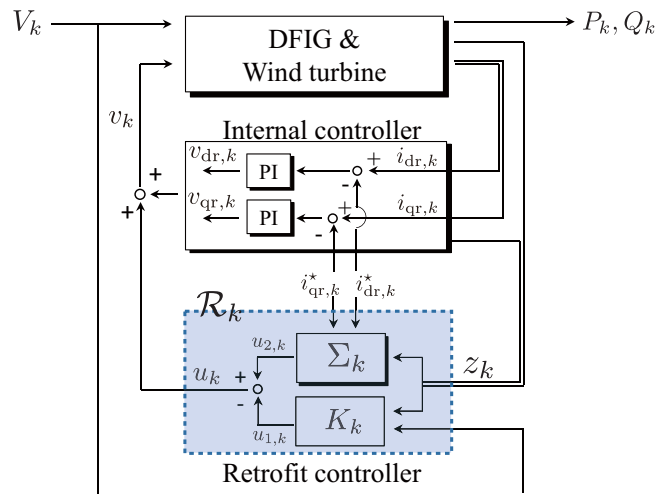

Fig. 7. Signal-flow diagram of wind farm with retrofit controller

where $f_k(z_k; i_{r,k}^\star) := F_k(z_k; i_{r,k}^\star) - A_k z_k$ and $\xi_k(0) = z_k^\star$, and implement u_k as in (13). The final controller can be written as the combination of (13), (15), and (16) as

$$\mathcal{R}_k : \begin{cases} \dot{\xi}_k = A_k \xi_k + f_k(z_k; i_{r,k}^\star) + R_k V_k \\ u_k = K_k(z_k - \xi_k). \end{cases} \tag{17}$$

Equation (17) is referred to as a *retrofit controller*. The following proposition holds for this controller.

Proposition 1: Let Assumptions 1 and 2 hold. Then, the interconnection of $\mathcal{P}$ and $\mathcal{R}_k$, $k \in \mathbb{N}_W$ in (17) is stable for any K_k such that $A_k + B_k K_k$ is Hurwitz.

The proof of Proposition 1 is briefly shown in the appendix. For a more detailed proof please refer to [10], [11]. The signal-flow diagram of the wind farm equipped with the retrofit controller is shown in Fig. 7. Proposition 1 shows that the retrofit controllers satisfy the stability requirement in Property (i) listed earlier. Furthermore, (17) shows that the controller satisfies Property (ii), i.e., $\mathcal{R}_k$ can be designed by using information of only $F_k(\cdot; \cdot)$, R_k, B_k and $z_k^\star$ of the k-th wind farm, which makes it modular, and $\mathcal{R}_k$ can be implemented by using feedback from only V_k, $i_{dr,k}^\star$ and $i_{qr,k}^\star$, which makes it decentralized. Neither the model nor the states of the "rest of the grid" are needed for designing or implementing $\mathcal{R}_k$.

Not just stability requirement in Property (i), the retrofit controller can also improve the dynamic performance of the wind farm by proper choice of the feedback gain K_k in (17), which can help in attenuating oscillations in the power flows. In fact, following [10], [11] we can show that there exists a class-$\mathcal{K}$ function (see [18] for definition of class-$\mathcal{K}$ functions) $\beta(\cdot)$ satisfying

$$\|\mathbf{z} - \mathbf{z}^\star\|_{\mathcal{L}_2} \leq \beta(\|\hat{\mathbf{z}}\|_{\mathcal{L}_2}) \tag{18}$$

where $\mathbf{z} \in \mathbb{R}^{9|\mathbb{N}_W|}$ and $\hat{\mathbf{z}} \in \mathbb{R}^{9|\mathbb{N}_W|}$ are the stacked representations of $z_k \in \mathbb{R}^9$ and $\hat{z}_k \in \mathbb{R}^9$ for $k \in \mathbb{N}_W$, and $\hat{z}_k$ obeys

$$\dot{\hat{z}}_k = (A_k + B_k K_k)\hat{z}_k, \quad \hat{z}_k(0) = (z_k(0) - z_k^\star). \tag{19}$$

Here, $\hat{z}_k$ represents wind farm behavior in response to a fault, whose impact is modeled by an impulsive shift in the initial

condition $z_k(0)$ from the equilibrium $z_k^\star$. The norm $\|\hat{\mathbf{z}}\|_{\mathcal{L}_2}$ can be shaped by any conventional optimal control design of u_k for example by Linear Quadratic Regulator (LQR) with a proper choice of K_k. Note that the choice of K_k for any wind farm is independent of that for all other wind farms. This provides a desired value of $\|\mathbf{z} - \mathbf{z}^\star\|_{\mathcal{L}_2}$, thereby improving the damping of the wind farm states, and, in turn, the damping of the electro-mechanical states of the pre-existing grid model. This theoretical guarantee for performance improvement is what distinguishes retrofit control from the current state-of-art wind power control methods, most of which are based on *adhoc* tuning of PID controllers. We summarize the main steps of the retrofit control design in the box below.

Steps for Constructing Retrofit Controllers

Initialization:
For $k \in \mathbb{N}_W$
1:    Given wind speed, find $P_k^\star$, $V_k^\star$ by MPPT
2:    Find $\theta_k^\star$, $k \in \mathbb{N}_W$ by power flow calculation
3:    Find $i_{r,k}^\star$ based on $P_k^\star$, $V_k^\star$, $\theta_k^\star$
4: Design PSS gains and PI gains of wind farms s.t. $\mathcal{P}$ is stable

Retrofit Controller Design:
For $k \in \mathbb{N}_W$
5:    Given $F_k(\cdot; i_{r,k}^\star)$, R_k, B_k in (12), $P_k^\star$, $Q_k^\star$ and $V_k^\star$, find $z_k^\star$
6:    Define A_k as in (14)
7:    Design K_k such that $A_k + B_k K_k$ is Hurwitz
8:    Implement $\mathcal{R}_k$ in (17)

A. Robustness Analysis

When the system operating conditions change, all setpoints starting from the setpoint for the mechanical power of each synchronous generator to the setpoints for the DFIG current generated by MPPT will change as well. In that situation, one may redesign the retrofit controllers based on these new setpoints following the steps listed above. However, it can be easily shown that even if such a redesign is not done, for instance to save time and effort, the retrofit controllers designed around the previous operating condition can still guarantee stability of the new closed-loop system, provided Assumptions 1 and 2 hold. In the following, we briefly describe this robustness property.

We denote the new setpoints by using the overbar, e.g., $\overline{i_{r,k}^\star}$ is the new setpoint of $i_{r,k}$. Under the same notations as above, the wind farm dynamics and retrofit controller can be described as

$$\dot{z}_k = F_k(z_k; \overline{i_{r,k}^\star}) + R_k V_k + B_k u_k, \qquad (20)$$

and

$$\overline{\mathcal{R}}_k : \begin{cases} \dot{\xi}_k = A_k \xi_k + (F_k(z_k; \overline{i_{r,k}^\star}) - A_k z_k) + R_k V_k \\ u_k = K_k(z_k - \xi_k) \end{cases}$$

$$(21)$$

respectively. Note that A_k and K_k in (21) are defined around the previous setpoint $z_k^\star$ while the model (20) is defined around the new setpoint $\overline{z_k^\star}$. However, if Assumption 1 is true, i.e., $\mathcal{P}$ is stable at the new setpoints with $u_k = 0$, then the term $F_k(z_k; \overline{i_{r,k}^\star}) - A_k z_k$ in (21) compensates the influence of using the previously linearized wind farm dynamics on the control input, thereby preserving stability of the closed-loop system. The proof follows the same argument as used in the proof for Proposition 1 in the appendix. The same coordinate transformation used in the proof can be applied to (20)-(21) to decouple the augmented wind dynamics from the rest of the system, and the Hurwitz property of $A_k + B_k K_k$ guarantees closed-loop stability for these new setpoints. The closed-loop performance, however, may degrade slightly depending on the difference between the old and new setpoints. Proper tuning of K_k can be used to improve this performance. The advantage is that unlike the PI-tuning described in Section III, in this case one will not have to worry about any instability resulting from a high or low value of K_k as long as $A_k + B_k K_k$ is stable. Also, the design of K_k for different wind farms can be done completely independently of each other.

B. Generalization to Low-dimensional Retrofit Controllers

Recall the IEEE 68-bus power system model with two wind farms, as shown in Section III. Let $\Psi_{w_1} \in \mathbb{R}^{9 \times 9}$ be the controllability Grammian of the first wind farm, determined by the pair of (A_{w_1}, B_{w_1}), where A_k and B_k are defined in (14) and (12). The eigenvalues of Ψ_{w_1} are 5.8×10^{-8}, 1.1×10^{-6}, 1.1×10^{-6}, 0.003, 0.029, 0.031, 0.033, 0.05, 0.07. The first three eigenvalues are significantly smaller than the others, indicating that at least three states of the DFIG model have poor controllability on the grid. The same is true for the second wind farm as well. This indicates that it is possible to reduce the dimension of the wind farm model, and thereby construct a lower-dimensional retrofit controller without significant loss of performance.

To design such low-dimensional retrofit controllers, we first define a tall matrix $W_k \in \mathbb{R}^{9 \times \hat{n}_k}$ of rank $\hat{n}_k \leq 9$ so that the state z_k of the wind farm can be approximated by a lower-dimensional vector $W_k^\dagger z_k$. A procedure for constructing W_k via balanced truncation will be shown shortly. The 9-dimensional retrofit controller $\mathcal{R}_k$ in (17) can then be generalized to an $\hat{n}_k$-dimensional retrofit controller

$$\hat{\mathcal{R}}_k : \begin{cases} \dot{\xi}_k = W_k^\dagger A_k W_k \xi_k + W_k^\dagger f_k(z_k; i_{r,k}^\star) + W_k^\dagger R_k V_k + \Gamma_k z_k \\ u_k = K_k W_k^\dagger z_k - K_k \xi_k \end{cases}$$

$$(22)$$

where K_k is designed so that $W_k^\dagger A_k W_k + W_k^\dagger B_k K_k$ is Hurwitz, $\Gamma_k := W_k^\dagger A_k(I_9 - W_k W_k^\dagger)$, and $\xi_k(0) = W_k^\dagger z_k^\star$. The variable $\Gamma_k z_k$ in (22) compensates the influence of the model reduction error on the control input $K_k W_k^\dagger z_k$. When $W_k = I_9$, this term vanishes as $\Gamma_k = 0$, and $\hat{\mathcal{R}}_k$ becomes same as $\mathcal{R}_k$. In that sense, $\hat{\mathcal{R}}_k$ is a generalization of $\mathcal{R}_k$ in (17).

One way of constructing W_k in (22) is to use balanced truncation with slight modification as shown in

[11]. Let U_k be a nonsingular matrix such that the triple $(U_k A_k U_k^{-1}, U_k B_k, U_k^{-1})$ is the balanced realization of the triple (A_k, B_k, I_9). Assume that the Hankel singular values of the system are arranged in descending order without loss of generality, and let $L \in \mathbb{R}^{9 \times m}$ be the first m columns of I_9. Then, for a sufficiently large value of m, W_k can be constructed as $W_k = U_k^{-1} G_k$, where G_k is given such that the subspace spanned by the columns of G_k is the same as that spanned by the columns of $[L, U_k B_k]$. The dimension $\hat{n}_k$ of the controller is then given by $m + \mathrm{rank}(B_k)$, which can be less than the dimension of z_k. The more uncontrollable Ψ_k is, the smaller will be the value of m. When Assumptions 1 and 2 hold, and $W_k^\dagger A_k W_k + W_k^\dagger B_k K_k$ is Hurwitz for $k \in \mathbb{N}_\mathrm{W}$, then the interconnection of $\mathcal{P}$ in Definition 1 and $\hat{\mathcal{R}}_k$ in (22) is stable.

C. Implementation in Individual Generators inside a Wind Farm

For realistic implementation, the controller (22) can be copied for each individual wind generator when the corresponding wind farm has multiple generators, assuming that $F_k(\cdot; \cdot)$, B_k, and R_k for the aggregate DFIG are the same as those of the individual DFIGs. The only requirement is that the states of every wind generator and the voltage magnitude V_k of the wind bus must be measurable. Even if the individual DFIG models are not identical, on the basis of the parallel interconnection structure of wind generators inside each wind farm, our controller can still be implemented as follows. For $h \in \{1, \ldots, \gamma_k\}$, let the h-th wind generator dynamics be defined as

$$\dot{z}_{k[h]} = F_{k[h]}(z_{k[h]}; i^\star_{\mathrm{r},k[h]}) + R_{k[h]} V_k + B_{k[h]} u_{k[h]}$$

where $z_{k[h]}$ is the wind generator state and $u_{k[h]}$ is an additional control input. Then, the retrofit controller for this generator is

$$\hat{\mathcal{R}}_{k[h]} : \begin{cases} \dot{\xi}_{k[h]} = W_{k[h]}^\dagger A_{k[h]} W_{k[h]} \xi_{k[h]} + W_{k[h]}^\dagger f_{k[h]}(z_{k[h]}; i^\star_{\mathrm{r},k[h]}) \\ \quad\quad + W_{k[h]}^\dagger R_{k[h]} V_k + \Gamma_{k[h]} z_{k[h]} \\ u_{k[h]} = K_{k[h]}(W_{k[h]}^\dagger z_{k[h]} - \xi_{k[h]}) \end{cases}$$

where $\Gamma_{k[h]} := W_{k[h]}^\dagger A_{k[h]}(I_9 - W_{k[h]} W_{k[h]}^\dagger)$ and $f_{k[h]}(z_{k[h]}; \cdot) := F_{k[h]}(z_{k[h]}; \cdot) - A_{k[h]} z_{k[h]}$. Again, the design of each retrofit controller can be done independently for each wind generator. The controllers do not need any communication among them. One advantage of this modular property is that in case the DFIG of a specific wind unit has strict saturation constraints then one does not need to tune every controller gain, but only the gain for that DFIG. Also note that during faults, the rotor side converter (RSC) is protected from the high currents induced in the machine using a crowbar [7]. When the the crowbar is activated, the operation of the RSC is interrupted. However, this interruption does not impact our controller in any way two reasons - first, the time-constant of the protection circuit is in milliseconds, and second, even when the RSC is interrupted the nominal PI controllers still remain functional.
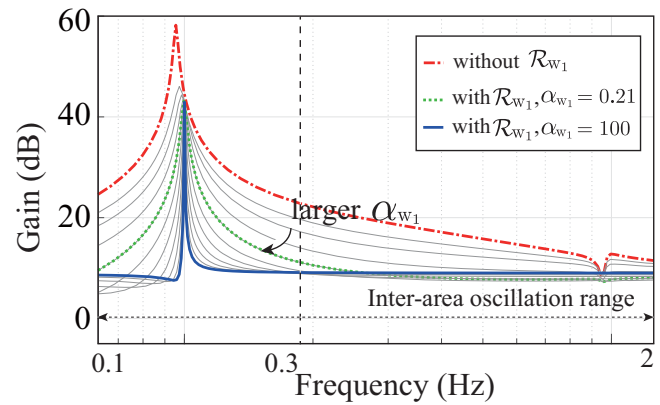

Fig. 8. Comparison of Bode gain diagram of wind farm 1 without and with retrofit controller for different values of α_{w_1}

V. NUMERICAL SIMULATIONS

In this section we show effectiveness of our proposed retrofit control by applying it to the wind-integrated IEEE 68-bus, 16-machine power system model shown in Fig. 2. For the rest of this section, the symbols with the subscript $_{\mathrm{W}_1}$ and $_{\mathrm{W}_2}$ denote the corresponding variables for the wind farm 1 and 2, respectively. The total generation capacity of the 16 synchronous generators is 18.4 GW. Let $\gamma_{\mathrm{w}_1} = 120$, $\gamma_{\mathrm{w}_2} = 100$. With each DFIG rated at 2 MW, the total wind generation capacity is then 440 MW, which is 2.4% of the total generated power. This may look like a small percentage, but in terms of the stability limit the amount of wind penetration is quite close to critical. As shown in Fig. 5, the value of γ_{w_1} beyond which the system becomes unstable is 150. Hence, the penetration level $\gamma_{\mathrm{w}_1} = 120$ should be considered high from a stability viewpoint.

As shown in Section III, high values of γ_{w_1} tend to stimulate a resonance peak in the frequency response of the rest of the grid, resulting in poorly damped inter-area oscillations in the line flows. Since this stimulation is primarily due to the oscillations of the power flowing out from the farm to the grid, the feedback gain K_{w1} in (17) is designed to mitigate the oscillations in the stator currents. To achieve this, we consider the isolated wind farm model in (19) with

$$[\hat{i}_{\mathrm{ds,w1}}, \hat{i}_{\mathrm{qs,w1}}]^\mathsf{T} = C_{\mathrm{w}_1} \hat{z}_{\mathrm{w1}} \quad\quad (23)$$

where $C_{\mathrm{w}_1} \in \mathbb{R}^{2 \times 9}$ is to select the stator currents around their operation point. For this model, we design K_{w_1} to minimize

$$J(K_{\mathrm{w}_1}) := \int_0^\infty (\alpha_{\mathrm{w}_1}(\hat{i}^2_{\mathrm{ds,w}_1}(t) + \hat{i}^2_{\mathrm{qs,w}_1}(t)) + \|K_{\mathrm{w}_1} \hat{z}_{\mathrm{w}_1}(t)\|^2) dt \quad\quad (24)$$

where α_{w_1} is a scalar weight. First, we design a retrofit controller $\mathcal{R}_{\mathrm{w}_1}$ in (17). The dimension of this resultant retrofit controller is nine, which is the same as the dimension of the wind farm model. A lower-dimensional controller will also be presented shortly.

We design several retrofit controllers for different values of α_{w_1} in (24), and show the closed-loop Bode gain diagram of wind farm 1 in Fig. 8. We can see from this figure that the gain at around 0.3 (Hz), which is the resonance frequency of
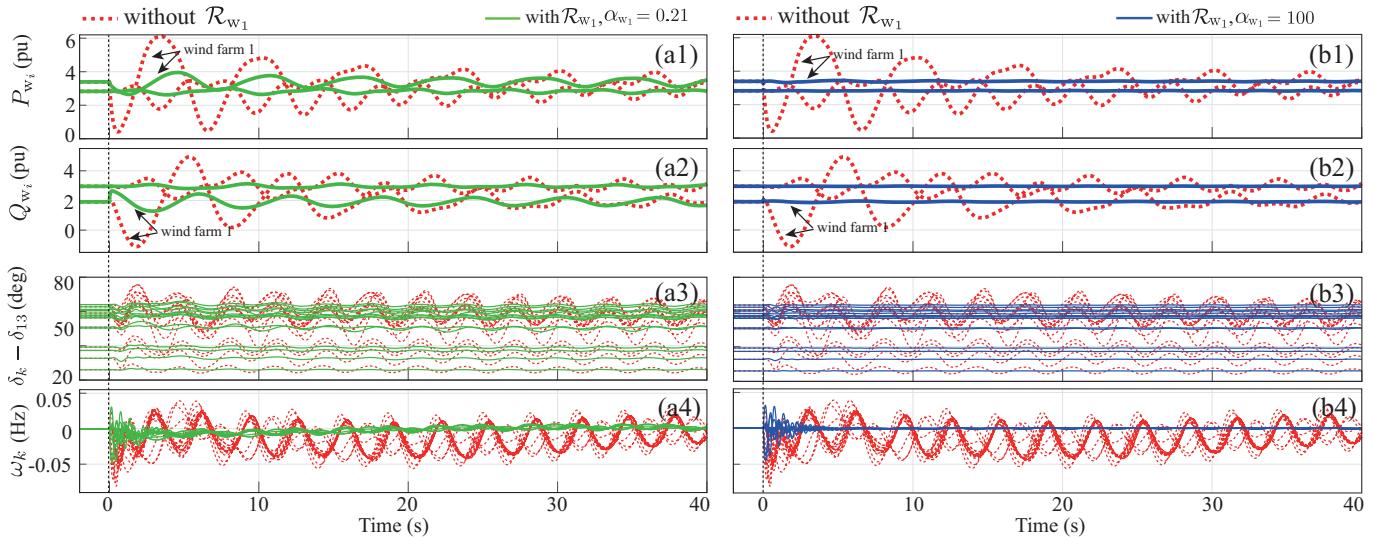
Fig. 9. Trajectories of active power output (top panel), reactive power output (second panel) of wind farm 1, angle differences (third panel), and frequencies (bottom panel) of synchronous generators for $\alpha_{w_1} = 0.21$ (left column) and $\alpha_{w_1} = 100$ (right column)

the grid excluding wind farm 1, is now getting smaller by increasing the value of α_{w_1}.

We next simulate the closed-loop performance of the wind-integrated system in response to a fault. We suppose the system to be in an equilibrium for $t < 0$. At $t = 0$ a fault happens, whose effect is modeled by an impulsive change in the DFIG current vector i_{w_1} from its equilibrium $i_{w_1}^\star$. The simulation is applied on the nonlinear model of the wind-integrated power system with $\mathcal{R}_{w_1}$. In Figs. 9(a1)-(a4), we show the active and reactive power output of the two wind farms, the phase angles of all synchronous generators relative to the swing generator (Generator 13 in this case) and the frequencies of all synchronous generators. The retrofit controller is designed for $\alpha_{w_1} = 0.21$. By comparing the red dotted and green solid lines in these subfigures, we can see that the large amount of open-loop resonant oscillations arising in both the wind and the grid states can be mitigated by using this control. Figs. 9(b1)-(b4), show the same responses for $\alpha_{w_1} = 100$, indicating that the damping performance of the closed-loop system can be significantly improved by making controller gain high. Assuming the cut-in slip to be at a standard value of 0.5 [19], the maximum power handled by the B2B converter can be considered to be roughly 7.5% of the power rating of the DFIG. i.e., the converter installed in each of the 120 wind generators should be rated at 150 KW. Usually, however, converters are rated at a much higher percentage, say 20-30% of the rating of the DFIG. Hence, for this system the converters installed in each wind generator should be roughly rated at 600 KW. From Figs. 9(a)-(b) we see that the maximum active power supplied by the DFIG of wind farm 1 during transience is 3.33 MW for $\alpha_{w_1} = 0.21$, and 2.87 MW for $\alpha_{w_1} = 100$. Accordingly, each converter should be able to handle at least 216 KW of power transfer in transience if the operator chooses to use $\alpha_{w_1} = 100$.

We quantify the performance improvement achieved by the retrofit control by a metric that computes the $\mathcal{L}_2$-norm of the

α_{w_1}	$Q_{improve}$	$\max_t \|v_{w_1}(t)\|$ (pu)
0.01	7.3302	0.2258
0.21	2.4524	0.3241
1.67	0.9661	0.3745
4.64	0.6105	0.4344
12.9	0.3932	0.5711
100	0.1774	1.3639

TABLE I
THE VALUE OF α_{w_1} IN (24), PERFORMANCE METRIC IN (25), AND MAXIMUM CONTROL INPUT OVER TIME.

generator frequencies $\omega(t) \in \mathbb{R}^{16}$ with respect to the worst-case perturbation of the DFIG current, i.e.,

$$Q_{improve} := \sup_{i_{w_1}(0) \in \mathbb{R}^4} \left(\frac{\|\omega\|_{\mathcal{L}_2}}{\|i_{w_1}(0) - i_{w_1}^\star\|} \right). \qquad (25)$$

Table I shows the variation of this metric with respect to α_{w_1} in (24). By comparing the first and second columns, we see that the damping performance of the generator frequencies improves consistently as the value of α_{w_1} increases. The trade-off, however, is that the amplitude of the control input in that case will be high as well. The third column of Table I shows the maximum control input over time. Higher values of the rotor voltage will require higher cost of insulation for the rotor windings. Too high controller gains can also instigate instability due to unmodeled dynamics in the wind model (12). The wind farm operator must choose the best α_{w_1} to balance these trade-offs with the closed-loop performance.

Next, we briefly investigate the robustness of the retrofit controller $\mathcal{R}_{w_1}$. For this, the active power consumption of the load at Bus 18 is changed from $P_{18}^\star = 2.47$ GW to $P_{18}^\star = 3.95$ GW. The DFIG current setpoints are updated accordingly, but A_{w_1} and K_{w_1} in (21) are not redesigned. In Fig. 10, the blue solid and red dotted lines show the frequencies of all synchronous generators for $P_{18}^\star = 2.47$ and $P_{18}^\star = 3.95$, respectively. We can see from this figure that
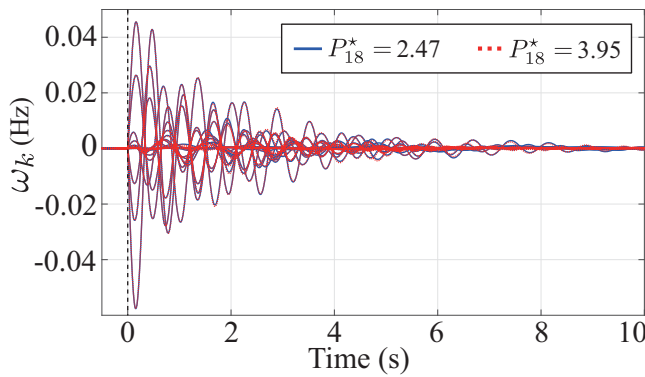
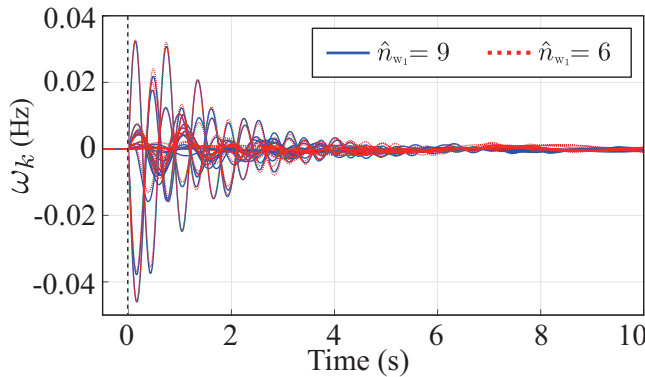Fig. 10. Robustness of retrofit controller against variation of load power

Fig. 11. Comparison of full-dimensional and low-dimensional retrofit controllers for the generator frequencies
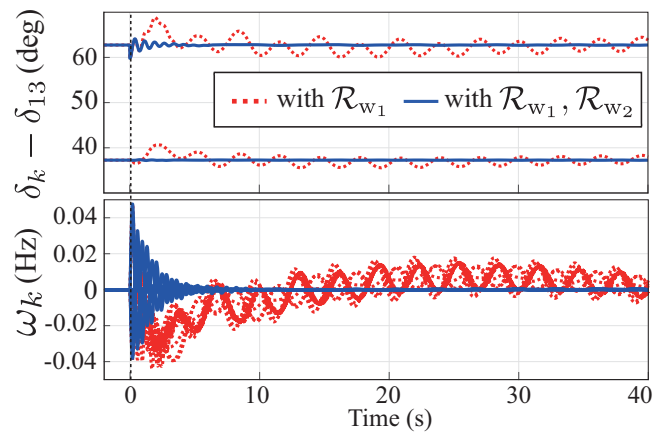

Fig. 12. Trajectories of (a) the angle of the generators nearest to wind farms (Generator 6 and 11), and (b) frequencies of all generators when the disturbance happens in wind farm 2.

$t > 0$.) Therefore, even if this controller is implemented in this scenario it does not have any influence on the closed-loop response. The red dotted lines in Fig. 12 point to this fact clearly. The second retrofit controller, on the other hand, improves damping as soon as it is activated. The design, therefore, enjoys a natural decoupling property from one farm to another, adding to the advantage of its decentralized implementation.

VI. CONCLUSION

In this paper we designed a set of decentralized controllers for DFIGs in a wind-integrated power system by which damping instabilities can be prevented for critical wind penetration levels. The advantage of the controller is that it does not require explicit knowledge of the dynamics of any part of the power system except for the wind farm itself, as a result of which it can be designed and implemented in a completely modular fashion. The effectiveness of the controllers in improving oscillation damping is verified by simulations of the IEEE 68-bus power system model. One drawback of the design is that we need an exact wind farm model as otherwise the closed-loop system stability is not theoretically guaranteed. One way to resolve this problem would be to use robust control theory to design the controller, which is a future work. Another drawback is that the decentralization of the design comes at the cost of the choice of fault locations. For example, here for simplicity we limited the spatial range of the incoming disturbance to inside the wind farm only as a result of which the design needed to know only the wind model. The more one intends to spread out the location of the buses where the fault may occur, the more will the design need to know the model for those bus variables, and thereby lose its decentralized property.

the controller designed at the previous operating condition is not only robustly stable, but also ensures almost the same performance as if it were redesigned.

We also investigate the effectiveness of the low-dimensional retrofit controller. The matrix W_{w_1} in (22) is designed according to the procedure in Section IV for $\hat{n}_{w_1} = 6$. Fig. 11 compares the generator frequencies for the 9-dimensional (blue solid) and 6-dimensional (red dotted) retrofit controllers. Comparing the plots we can easily see that the lower-dimensional controller performs almost as effectively as the higher-dimensional controller does.

Finally, we investigate how the power system behaves when we plug in a second retrofit controller, namely at wind farm 2, while retaining the retrofit controller at wind farm 1. The design of the second retrofit controller $\mathcal{R}_{w_2}$ follows the same procedure taken for designing $\mathcal{R}_{w_1}$. In Fig. 12 we show trajectories of the relative angles and frequencies of the generators that are nearest to the two wind farms, when a fault happens at $t = 0$ inside wind farm 2. The red dotted lines show the response when only the retrofit controller at wind farm 1 is implemented. The blue solid lines show the response when the retrofit controllers for both wind farms 1 and 2 are implemented. Note that when a fault happens in wind farm 2 the first retrofit control input is identically zero for all time $t > 0$ (this follows from (27) in the appendix. Since $\hat{z}_{w_1}(0) = 0$, we get $u_{w_1}(t) \equiv K_{w_1}\hat{z}_{w_1}(t) \equiv 0$ for any

$$A_{\mathrm{i},k}(\omega_{\mathrm{g},k}) = \frac{1}{\Phi_k} \begin{bmatrix} -r_{\mathrm{r},k}x_{\mathrm{s},k} & \Phi_k - \omega_{\mathrm{g},k}x_{\mathrm{s},k}x_{\mathrm{r},k} & r_{\mathrm{s},k}x_{\mathrm{m},k} & -\omega_{\mathrm{g},k}x_{\mathrm{s},k}x_{\mathrm{m},k} \\ -\Phi_k + \omega_{\mathrm{g},k}x_{\mathrm{s},k}x_{\mathrm{r},k} & -r_{\mathrm{r},k}x_{\mathrm{s},k} & \omega_{\mathrm{g},k}x_{\mathrm{s},k}x_{\mathrm{m},k} & r_{\mathrm{s},k}x_{\mathrm{m},k} \\ r_{\mathrm{r},k}x_{\mathrm{m},k} & \omega_{\mathrm{g},k}x_{\mathrm{r},k}x_{\mathrm{m},k} & -r_{\mathrm{s},k}x_{\mathrm{r},k} & \Phi_k + \omega_{\mathrm{g},k}x_{\mathrm{m},k}^2 \\ -\omega_{\mathrm{g},k}x_{\mathrm{r},k}x_{\mathrm{m},k} & r_{\mathrm{r},k}x_{\mathrm{m},k} & -\Phi_k - \omega_{\mathrm{g},k}x_{\mathrm{m},k}^2 & -r_{\mathrm{s},k}x_{\mathrm{r},k} \end{bmatrix}, \quad B_{\mathrm{i},k} = \frac{1}{\Phi_k} \begin{bmatrix} -x_{\mathrm{s},k} & 0 \\ 0 & -x_{\mathrm{s},k} \\ x_{\mathrm{m},k} & 0 \\ 0 & x_{\mathrm{m},k} \end{bmatrix}$$

$$R_{\mathrm{i},k} = \frac{1}{\Phi_k} \begin{bmatrix} 0 & x_{\mathrm{m},k} & 0 & -x_{\mathrm{r},k} \end{bmatrix}^{\mathsf{T}}$$

$$\tag{28}$$

$$A_{\mathrm{pss},k} = \begin{bmatrix} -\frac{1}{\tau_{\mathrm{pss},k}} & 0 & 0 \\ -\frac{K_{\mathrm{pss},k}}{\tau_{\mathrm{pss},k}\tau_{\mathrm{L1},k}}\left(1 - \frac{\tau'_{\mathrm{L1},k}}{\tau_{\mathrm{L1},k}}\right) & -\frac{1}{\tau_{\mathrm{L1},k}} & 0 \\ -\frac{K_{\mathrm{pss},k}\tau'_{\mathrm{L1},k}}{\tau_{\mathrm{pss},k}\tau_{\mathrm{L1},k}\tau_{\mathrm{L2},k}}\left(1 - \frac{\tau'_{\mathrm{L2},k}}{\tau_{\mathrm{L2},k}}\right) & \frac{1}{\tau_{\mathrm{L2},k}}\left(1 - \frac{\tau'_{\mathrm{L2},k}}{\tau_{\mathrm{L2},k}}\right) & -\frac{1}{\tau_{\mathrm{L2},k}} \end{bmatrix}, \quad B_{\mathrm{pss},k} = \begin{bmatrix} \frac{1}{\tau_{\mathrm{pss},k}} \\ \frac{K_{\mathrm{pss},k}}{\tau_{\mathrm{pss},k}\tau_{\mathrm{L1},k}}\left(1 - \frac{\tau'_{\mathrm{L1},k}}{\tau_{\mathrm{L1},k}}\right) \\ \frac{K_{\mathrm{pss},k}\tau'_{\mathrm{L1},k}}{\tau_{\mathrm{pss},k}\tau_{\mathrm{L1},k}\tau_{\mathrm{L2},k}}\left(1 - \frac{\tau'_{\mathrm{L2},k}}{\tau_{\mathrm{L2},k}}\right) \end{bmatrix}$$

$$C_{\mathrm{pss},k} = \begin{bmatrix} -\frac{K_{\mathrm{pss},k}\tau'_{\mathrm{L1},k}\tau'_{\mathrm{L2},k}}{\tau_{\mathrm{pss},k}\tau_{\mathrm{L1},k}\tau_{\mathrm{L2},k}} & \frac{\tau'_{\mathrm{L2},k}}{\tau_{\mathrm{L2},k}} & 1 \end{bmatrix}, \qquad D_{\mathrm{pss},k} = \frac{K_{\mathrm{pss},k}\tau'_{\mathrm{L1},k}\tau'_{\mathrm{L2},k}}{\tau_{\mathrm{pss},k}\tau_{\mathrm{L1},k}\tau_{\mathrm{L2},k}} \tag{29}$$

APPENDIX

A. State-space matrices for DFIG and PSS

Mathematical expressions for the different matrices constituting the DFIG state-space model in (7) are provided in equation (28). Matrices for the PSS model in (4) are provided in equation (29) where $K_{\mathrm{pss},k}$ is the PSS gain, $\tau_{\mathrm{pss},k}$ is the washout filter time constant (sec), $\tau_{\mathrm{L1},k}$ and $\tau'_{\mathrm{L1},k}$ are the lead-lag time constants of the first stage of PSS feedback (sec), and $\tau_{\mathrm{L2},k}, \tau'_{\mathrm{L2},k}$ are the lead-lag time constants of the second stage of PSS feedback (sec).

B. Power System Model Parameters

For $k \in \mathbb{N}_{\mathrm{W}}$, the parameters of the wind turbine in (6) are summarized as follows: $J_{\mathrm{r},k} = 1.95 \times 10^4$, $J_{\mathrm{g},k} = 1.39 \times 10^{-1}$, $B_{\mathrm{r},k} = 9.88$, $B_{\mathrm{g},k} = 1.10 \times 10^{-3}$, $K_{\mathrm{c},k} = 5.09 \times 10^2$, $d_{\mathrm{c},k} = 3.36 \times 10^{-2}$, $P_{\mathrm{a},k} = 2.5 \times 10^{-2}$, and $N_{\mathrm{g},k} = 90$. Note that all the values are rated at the system capacity 100 MW. The parameters of DFIG rated at 2 MW and 690 V in (7) and (28) are $x_{\mathrm{s},k} = 4.03$, $x_{\mathrm{r},k} = 4.03$, $r_{\mathrm{s},k} = 0.01$, $r_{\mathrm{r},k} = 0.001$, $x_{\mathrm{m},k} = 4.0$, and $\Phi_k := x_{\mathrm{s},k}x_{\mathrm{r},k} - x_{\mathrm{m},k}^2$. The synchronous generator model and tie-line parameters are as in the IEEE 68-bus system prototype model. For any $k \in \mathbb{N}_{\mathrm{G}}$, the parameters of PSS in (29) are $K_{\mathrm{pss},k} = 500$, $\tau_{\mathrm{pss},k} = 10$, $\tau_{\mathrm{L1},k} = 0.02$, $\tau'_{\mathrm{L1},k} = 0.07$, $\tau_{\mathrm{L2},k} = 0.02$, and $\tau'_{\mathrm{L2},k} = 0.07$.

C. Proof of Proposition 1

From the definition of $\mathcal{P}$, the wind bus voltage V_k in (12) can be expressed as

$$V_k = \mathcal{G}_k(\{z_k\}_{k \in \mathbb{N}_{\mathrm{W}}}) \tag{26}$$

where $\mathcal{G}_k(\cdot)$ is a dynamical map and $\{z_k\}_{k \in \mathbb{N}_{\mathrm{W}}}$ is the set of z_k in (12) for $k \in \mathbb{N}_{\mathrm{W}}$. Considering the coordinate transformation $\hat{z}_k := z_k - \xi_k$, we get

$$\begin{cases} \dot{\hat{z}}_k = (A_k + B_k K_k)\hat{z}_k \\ \dot{\xi}_k = F_k(\xi_k + \hat{z}_k; i^\star_{\mathrm{r},k}) + R_k V_k - A_k \hat{z}_k. \end{cases} \tag{27}$$

Clearly, $\lim_{t \to \infty} \hat{z}_k(t) = 0$ because K_k is designed such that $A_k + B_k K_k$ is Hurwitz. Hence, $\lim_{t \to \infty} u_k(t) = \lim_{t \to \infty} K_k \hat{z}_k(t) = 0$. Furthermore, the dynamics of ξ_k in (27) with $V_k = \mathcal{G}_k(\{\xi_k + \hat{z}_k\}_{k \in \mathbb{N}_{\mathrm{W}}})$ at $\hat{z}_k = 0$ is the same as the dynamics of the wind-integrated power system $\mathcal{P}$ under $u_k \equiv 0$. Hence, by Assumption 1 and the fact that $\hat{z}_k$ does not depend on ξ_k, we get $\lim_{t \to \infty} \xi_k(t) = \xi^\star_k$. Note that $\xi^\star_k = z^\star_k$ and $z_k = \xi_k + \hat{z}_k$. Hence, $\lim_{t \to \infty} z_k = \lim_{t \to \infty} \xi_k(t) = z^\star_k$, implying that the power flow converges to its desired equilibrium.

REFERENCES

[1] E. Vittal, M. O'Malley, and A. Keane, "Rotor angle stability with high penetrations of wind generation," *IEEE Transactions on Power Systems*, vol. 27, no. 1, pp. 353–362, 2012.

[2] E. Vittal, C. Cuffe, and A. Keane, "Transient stability impacts from distribution connected wind farms," in *IEEE Power and Energy Society General Meeting*, 2012, pp. 1–5.

[3] S. Chandra, D. Mehta, and A. Chakrabortty, "Exploring the impact of wind penetration on power system equilibrium using a numerical continuation approach," in *Proc. American Control Conference*, 2015, pp. 4339–4344.

[4] D. Gautam, V. Vittal, and T. Harbour, "Impact of increased penetration of dfig-based wind turbine generators on transient and small signal stability of power systems," *IEEE Transactions on Power Systems*, vol. 24, no. 3, pp. 1426–1434, 2009.

[5] G. Di Marzio, O. Fosso, K. Uhlen, and M. Pálsson, "Large-scale wind power integration-voltage stability limits and modal analysis," in *Proc. Power System Computation Conference*, vol. 16, no. 3, 2005, pp. 1–7.

[6] S. Chandra, D. Gayme, and A. Chakrabortty, "Time-scale modeling of wind-integrated power systems," *IEEE Transactions on Power Systems*, vol. 31, no. 6, pp. 4712–4721, 2016.

[7] T. Ackerman, *Power Wind Power in Power Systems*. John Wiley & Sons, 2005.

[8] V. Vittal and R. Ayyanar, *Grid Integration and Dynamic Impact of Wind Energy*. Springer-Verlag New York, 2013.

[9] T. Sadamoto, A. Chakrabortty, T. Ishizaki, and J. Imura, "A retrofitting-based supplementary controller design for enhancing damping performance of wind power systems," in *Proc. American Control Conference*, 2017, pp. 2755–2760.

[10] T. Ishizaki, T. Sadamoto, J. Imura, H. Sandberg, and K. H. Johansson, "Retrofit control: Localization of controller design and implementation," Available at: https://arxiv.org/abs/1611.04531.

[11] T. Sadamoto, T. Ishizaki, J. Imura, H. Sandberg, and K. H. Johansson, "Retrofitting state feedback control of networked nonlinear systems based on hierarchical expansion," in *Proc. IEEE Conference on Decision and Control*, 2016, pp. 3432–3437.

[12] G. Rogers, *Power system oscillations*. Springer Science & Business Media, 2012.

[13] P. Kundur, *Power system stability and control*. McGraw-Hill Education, 1994.

[14] V. Akhmatov and H. Knudsen, "An aggregate model of a grid-connected, large-scale, offshore wind farm for power stability investigations-importance of windmill mechanical system," *International Journal of Electrical Power & Energy Systems*, vol. 24, no. 9, pp. 709–717, 2002.

[15] H. Nikkhajoei and R. Iravani, "Dynamic model and control of ac–dc–ac voltage-sourced converter system for distributed resources," *IEEE Transactions on Power Delivery*, vol. 22, no. 2, pp. 1169–1178, 2007.

[16] C. Sloth, T. Esbensen, and J. Stoustrup, "Active and passive fault-tolerant lpv control of wind turbines," in *Proc. American Control Conference*. IEEE, 2010, pp. 4640–4646.

[17] C. E. Ugalde-Loo, J. B. Ekanayake, and N. Jenkins, "State-space modeling of wind turbine generators for power system studies," *IEEE Transactions on Industry Applications*, vol. 49, no. 1, pp. 223–232, 2013.

[18] H. K. Khalil, *Nonlinear systems*. Prentice hall New Jersey, 1996, vol. 3.

[19] S. Halim and E. Naguib, "Sizing of converters interfacing the rotor of wind driven dfig to the power grid," *Smart Grid and Renewable Energy*, vol. 2, pp. 300–304, 2011.
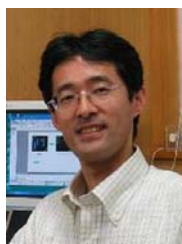
Tomonori Sadamoto (M'15) was born in Chiba, Japan, in 1987. He received Ph.D. from Tokyo Institute of Technology in 2015. Since April in 2016 to August in 2016, he was a researcher with the Department of Systems and Control Engineering Graduate School of Engineering, Tokyo Institute of Technology. Since August in 2016, he is currently a specially appointed assistant professor with the same department in Tokyo Institute of Technology. He is a member of IEEE, SICE, and ISCIE.

Aranya Chakrabortty (M'08, SM'15) received his PhD degree in Electrical Engineering from Rensselaer Polytechnic Institute, Troy, NY in 2008. From 2008 to 2009 he was a postdoctoral research associate at the Aeronautics and Astronautics department of University of Washington, Seattle. He is currently an Associate Professor in the Electrical and Computer Engineering department of North Carolina State University, Raleigh, NC, where he is also affiliated to the FREEDM Systems Center. His research interests are in all branches of control theory with applications to power systems, especially in wide-area monitoring and control of large power systems using Synchrophasors. He received the NSF CAREER award in 2011.

Takayuki Ishizaki was born in Aichi, Japan, in 1985. He received the B.Sc., M.Sc., and Ph.D. degrees in engineering from Tokyo Institute of Technology, Tokyo, Japan, in 2008, 2009, and 2012, respectively. Since November 2012, he has been with the Department of Mechanical and Environmental Informatics, Graduate School of Information Science and Engineering, Tokyo Institute of Technology, where he is currently an Assistant Professor. Dr. Ishizaki is a member of IEEE, SICE, and ISCIE. He was named as a finalist of the 51st IEEE CDC Best Student-Paper Award.

Jun-ichi Imura (M'93) was born in Gifu, Japan, in 1964. He received the Ph.D. degree in mechanical engineering from Kyoto University, Kyoto, Japan, in 1995. Since 2001, he has been with the Department of Mechanical and Environmental Informatics, Graduate School of Information Science and Engineering, Tokyo Institute of Technology, Tokyo, Japan, where he is currently a Professor. Dr. Imura is a member of IEEE, SICE, ISCIE, IEICE, and The Robotics Society of Japan.